Computerized Tomography and Nuclear Magnetic Resonance

L. A. Shepp

Abstract: In 1917 Radon gave a simple formula for reconstructing a function $f(x,y,z)$ from its integrals over all planes in three-dimensions. We give a simple algorithm for numerical quadrature of his formula and suggest its application to imaging the nuclear magnetic resonance spin density of an object. **Index Terms:** Nuclear magnetic resonance—Image reconstruction—Data processing.

1. INTRODUCTION

The theoretical basis of X-ray computerized tomography (XCT) is the mathematical theorem of Radon (1) that a function $f(x,y)$ can be uniquely reconstructed from its line integrals in the x-y plane. If f represents the X-ray density in one plane section of a real object such as a human head, the *line* integrals of the density can be approximated by measuring the attenuation of an X-ray beam passed along the various lines. The resulting reconstruction image of f by XCT has become an important tool in diagnostic radiology.

Nuclear magnetic resonance (NMR) measurements can be used to approximate the *plane* integrals of the density $f(x,y,z)$ of hydrogen nuclei in a real object. We will show that these measurements can also be used to reconstruct and image the density f. (Note that the X-ray density and the hydrogen density are different, although roughly proportional except in bone.) Indeed, in the same paper (1), Radon proved that a function $f(x,y,z)$, continuous and of compact support, can be uniquely reconstructed from its plane integrals by an explicit formula. We give a simple numerical algorithm (Section 2) for the approximate reconstruction of f from a natural finite set of plane integrals of f. This gives an explicit procedure for obtaining an NMR computerized tomography (NCT) image of f which is completely analogous to that of XCT. NCT has time-resolution advantages over so-called direct techniques in NMR imaging which do

not use the full resonance NMR signal as discussed below.

Let $f(x,y,z)$ represent the spin density of atomic nuclei of a given spin type (say hydrogen) at each point (x,y,z) of an object, say a human head. In NCT, a space-varying magnetic field is imposed in the space containing the object. The level surfaces of the magnetic field are approximately a series of parallel planes. After excitation by a broad-band radiofrequency pulse, each nucleus precesses at a rate proportional to the magnetic field strength at its point of location. Thus the total magnetic energy at any given frequency represents the integral of the spin density over the surface of constant magnetic field corresponding to this frequency. In this way the plane integrals of f can be approximated. This method of measuring plane integrals of the spin density is known as the gradient method.

The idea of mathematical inversion of the NMR measured plane integrals is not new. In fact, it is well known (2–5) that the plane integrals of f actually determine f via the Fourier projection theorem (3) (i.e., the fact that the one-dimensional Fourier transform of the plane integrals normal to any one line is the three-dimensional Fourier transform $\hat{f}$ of f along the line). The general problem of inverting the NMR projection data to reconstruct f has been called zeugmatography (2), and attempts have been made to reconstruct from planar projections by a double use of the linear projection technique (2). However, it was observed (3,5) that the technique of determining f by first determining $\hat{f}$ using the projection theorem is clumsy, indirect, and inaccurate (and the double use of linear reconstruction is not much simpler). Indeed the use of

mathematical inversion has apparently been intentionally ignored (5) in NMR imaging. On the other hand, there is much interest in NMR diagnostic imaging because NMR is nonionizing and noninvasive in contrast with XCT (6) (and allows for an easier interaction with metabolic processes than XCT), and so NMR imaging is an active field. Most researchers, however, rely on "direct" techniques. These direct techniques use one or more methods of *physically* canceling the superposition effect of forming plane integrals by using either (a) rapidly switched magnetic field gradients, intended to cancel the contribution of spins outside a sensitive region, usually a point (5), or (b) narrow-band radiofrequency excitation pulses, intended to either excite, or to saturate, only the spins in a limited region (4).

The above direct techniques avoid the need for mathematical inversion but have the disadvantage that only a small volume of the object is actually radiating spin energy due to the selectivity of the technique. The signal-to-noise ratio is thereby decreased by a factor approximately equal to the ratio of excited volume to total volume. Thus mathematical inversion has advantages in decreasing data acquisition time when it is desired to reconstruct *the entire object*. This time limitation is critical because of the long ($\sim$1 sec) spin relaxation times.

In Section 2 we give the mathematical basis of NCT and also a simple algorithm and simple FORTRAN program (Appendix A) for reconstructing from a set of parallel plane measurements. In Section 3 we give an experimental simulation using a model of a human head made of ellipsoids where the projection data can be exactly calculated under ideal and noise conditions in order to separate algorithmic effects from those due to erroneous data and to compare the resolution with that of XCT (7,8).

We find that there are many interesting parallels with linear algorithms in XCT. To obtain a resolution roughly equivalent to that of the XCT simulation experiments described in the work of Shepp and Logan (8) requires about 100 times as many projections: 5,000–10,000 compared to 50–100 in XCT. Here a projection is thought of as a set of (say 100) parallel planes. This is partly due to the fact that realistic head phantoms include high-contrast objects outside the plane (nose, ears, mouth, etc.) which "cast tangents" (due to their edges) inside the plane of reconstruction. On the other hand, this increased number of projections should perhaps have been expected, since these same projections now allow reconstruction in *all slice planes at once*. Further, as we shall see, the mathematics of NCT is even simpler than that of XCT.

2. RADON'S INVERSION OF f FROM PLANE INTEGRALS

Let $f = f(x,y,z)$ be continuous and of compact support. For each unit vector u and $-\infty < t < \infty$ let $\mathcal{P}(t,u)$ denote the plane whose normal from the origin is tu. The plane integral

$$P(t,u) = \int_{\mathcal{P}(t,u)} f \, dA \qquad (2.1)$$

is the two-dimensional projection of f along $P(t,u)$. Note that $\mathcal{P}(-t,-u) = P(t,u)$, and hence $\mathcal{P}(-t,-u) = P(t,u)$.

Radon (1) gave an inversion formula for f in terms of P as follows. First he defines for each point $Q = (x,y,z)$ the point mean value of P over all planes through Q,

$$F(Q) = \frac{1}{4\pi} \iint_{u\in S} P(t(Q),u) \, dS(u) \qquad (2.2)$$

where $u\in S$ means that u runs over the unit sphere S of unit vectors with $dS(u)$ the local element of area on S and $t(Q)$ being the value of t for which $P(t,u)$ contains the point Q. Since $F(Q)$ represents a fourfold integration of f, it reduces to a threefold integral of f, as is easy to see: namely,

$$F(Q) = F(x,y,z)$$

$$= \frac{1}{2} \iiint_{-\infty}^{\infty} f(x',y',z') \frac{dx' \, dy' \, dz'}{[(x-x')^2 + (y-y')^2 + (z-z')^2]^{1/2}}$$

$$\qquad (2.3)$$

so that $F(Q)$ is the same as the convolution of f with $(1/2r)$, $F = \frac{1}{2} f * r^{-1}$. But then $2F$ is the analog of the electrostatic potential due to an electric charge density f, so by Gauss' formula (9), $f = -(1/4\pi) \nabla^2 (f * r^{-1})$, we have

$$f(x,y,z) = -\frac{1}{2\pi} \left(\frac{\partial^2}{\partial x^2} + \frac{\partial^2}{\partial y^2} + \frac{\partial^2}{\partial z^2} \right) F(x,y,z) . \qquad (2.4)$$

Since F is given in Eq. 2.2 in terms of $P(t,u)$, Eq. 2.4 gives the (Radon's) formula for reconstructing f from P.

One interesting consequence of Eq. 2.4 is that to reconstruct $f(Q)$ it is not necessary to use all values of $P(t,u)$, but only those values for planes $\mathcal{P}$ passing through an arbitrarily small sphere about Q. This localization property of the reconstruction of f from plane integrals has no counterpart in XCT, where *all* line integrals are used (8,10) to reconstruct f at any one point. In this sense, the NCT reconstruction formula is simpler than in the XCT case. On the other hand, it does not seem convenient with the gradient technique to obtain localized data without actually being in a position to obtain the full set of data.

As in the linear case (10), Radon's formula is not directly suited to a numerical implementation, since it is awkward to form Eq. 2.2 as an intermediate step to Eq. 2.4. A different reconstruction formula based on

Fourier transforms seems to give more insight. However, an alternative algorithm based on Eqs. 2.2 and 2.4 is considered at the end of this section.

Introducing spherical coordinates, $0 \le \theta \le \pi, 0 \le \alpha \le 2\pi$ and setting $P(t,\theta,\alpha) = P(t,\mathbf{u})$, where

$$\mathbf{u} = (\sin\theta \cos\alpha, \sin\theta \sin\alpha, \cos\theta) \qquad (2.5)$$

we define

$$\hat{P}(\omega,\theta,\alpha) = \int_{-\infty}^{\infty} P(t,\theta,\alpha) \exp(-i\omega t)\, dt \qquad (2.6)$$

It is easy to see that

$$\hat{P}(\omega,\theta,\alpha) = \hat{f}(\omega,\theta,\alpha) \qquad (2.7)$$

where $\hat{f}$ is the three-dimensional Fourier transform of f,

$$\hat{f}(\omega,\theta,\alpha) = \iiint_{-\infty}^{\infty} f(x,y,z) \exp\{-i\omega[(x \cos\alpha$$

$$+ y \sin\alpha)\sin\theta + z \cos\theta]\}\, dx\, dy\, dz. \qquad (2.8)$$

The Fourier inversion formula [and $\hat{f}(-\omega,\theta,\alpha) = \hat{f}(\omega,\theta,\alpha)*$] then gives

$$f(x,y,z) = \left(\frac{1}{2\pi}\right)^3 \int_0^{2\pi} d\alpha \int_0^{\pi} d\theta \int_0^{\infty}$$

$$d\omega\, \hat{f}(\omega,\theta,\alpha)\omega^2 \sin\theta \exp(i\omega t)$$

$$= \left(\frac{1}{2\pi}\right)^3 \frac{1}{2}\int_0^{2\pi} d\alpha \int_0^{\pi} d\theta \int_{-\infty}^{\infty}$$

$$d\omega\, \hat{f}(\omega,\theta,\alpha)\omega^2 \sin\theta \exp(i\omega t) \qquad (2.9)$$

where

$$t = x \sin\theta \cos\alpha + y \sin\theta \sin\alpha + z \cos\theta. \qquad (2.10)$$

From Eq. 2.6, the one-dimensional Fourier inversion formula gives

$$P(t,\theta,\alpha) = \frac{1}{2\pi}\int_{-\infty}^{\infty} \hat{P}(\omega,\theta,\alpha) \exp(i\omega t)\, d\omega \qquad (2.11)$$

Differentiating (2.11) twice on t, formally, we obtain

$$-P''(t,\theta,\alpha) = \frac{1}{2\pi}\int_{-\infty}^{\infty} \hat{P}(\omega,\theta,\alpha)\omega^2 \exp(i\omega t)\, d\omega \quad (2.12)$$

Using Eq. 2.7 in Eqs. 2.9 and 2.12, we get simply

$$f(x,y,z) = -\frac{1}{8\pi^2}\int_0^{2\pi} d\alpha \int_0^{\pi} d\theta\, P''(t,\theta,\alpha) \sin\theta$$

$$(2.13)$$

where t is given in Eq. 2.10 and represents the distance from the origin to the plane $\mathcal{P}(t,\mathbf{u}) = \mathcal{P}(t,\theta,\alpha)$ containing the point (x,y,z). Of course, Eq. 2.13 must be the same as Eq. 2.4 whenever P is sufficiently smooth so that the above differentiations may be performed. On the other hand, Eq. 2.13 shows more clearly than Eq. 2.4 how each measured plane integral $P(t,\theta,\alpha)$ contributes to the reconstruction at (x,y,z). In fact, Eq. 2.13 is exactly in the same form as in XCT (8,10), i.e., f is a filtered back-

projection of P where the filter realizes the operation of second-order differentiation by a second-order difference. Thus the filter here is a three-point (local) filter, whereas in XCT the filter involves all the points (8,10).

Equation 2.13 suggests the following natural algorithm for the physically natural case where for each of N directions $\mathbf{u}_1, \ldots, \mathbf{u}_N$ we are given the planar projections of f along equispaced parallel planes. No set of directions seems completely natural, and the one we have chosen is arbitrary; but for definiteness we assume $P(t_l,\theta_j,\alpha_k)$ is known for $\theta_j = ((j-\frac{1}{2})\pi/n), j = 1, \ldots, n;$ $\alpha_k = (k2\pi/m), k = 0, \ldots, m - 1;$ and $t_l = la, l = 0, \pm 1, \pm 2, \ldots$ We then set as our approximation to $f(x,y,z)$ in (2.13)

$$\bar{f}(x,y,z) = \frac{1}{4mn} \sum_{j=1}^{n} \sum_{k=0}^{m-1} \sin\theta_j\, Q(t,\theta_j,\alpha_k) \qquad (2.14)$$

where

$$t = x \sin\theta_j \cos\alpha_k + y \sin\theta_j \sin\alpha_k + z \cos\theta_j \quad (2.15)$$

and Q is the natural second-difference approximation to $-P''$,

$$Q(t_l,\theta,\alpha) = a^{-2}[2P(t_l,\theta,\alpha) - P(t_{l-1},\theta,\alpha) - P(t_{l+1},\theta,\alpha)] \qquad (2.16)$$

at $t = t_l$ and is extended linearly in the intervals $t_l < t < t_{l+1}$. The FORTRAN program which realizes reconstruction 2.14 and generates the data $P(t_l,\theta_j,\alpha_k)$ for the phantom used in the experiments described below is given in Appendix A.

Radon's formula (2.2) and Eq. 2.4 lead to a slightly less convenient algorithm in which we first back-project $P(t,\theta,\alpha)$ to obtain an approximation to $F(x,y,z)$ in Eq. 2.2 and then apply the Laplacian difference operator to approximate f in Eq. 2.4. Thus we first form

$$\bar{F}(x,y,z) = \frac{1}{4\pi} \frac{\pi}{n} \frac{2\pi}{m} \sum_{j=1}^{n} \sum_{k=0}^{m-1} \sin\theta_j\, P(t,\theta_j,\alpha_k) \quad (2.17)$$

where $P(t_l,\theta_j,\alpha_k)$ is the measured or calculated value at the sample points $t = t_l$ and $P(t,\theta_j,\alpha_k)$ is the linear interpolation. We then form the second-order difference approximation to the Laplacian (2.4),

$$\bar{\bar{f}}(x,y,z) = \frac{1}{2\pi a^2}\left[2F(x,y,z) - F(x+a,y,z) - F(x-a,y,z)\right.$$

$$+ 2F(x,y,z) - F(z,y+a,z) - F(x,y-a,z)$$

$$\left. + 2F(x,y,z) - F(x,y,z+a) - F(x,y,z-a)\right]. \qquad (2.18)$$

This algorithm is more difficult to program and is less elegant in that one must (arbitrarily) choose the x,y,z axes to define the second-order approximation in (2.18). Further the effective back-projection in each direction is much more oscillatory than with f in (2.14). As a consequence one would not expect good performance from $\bar{\bar{f}}$, which is the case in the experiments made in the following section.

3. SIMULATION EXPERIMENTS

In order to compare the resolution achievable

FIG. 1. Section of original phantom $z = 0.381$.

with the planar (Eq. 2.14) and linear (Eq. 12 in ref. 8) algorithms, we simulated a three-dimensional head which in fact extends the head phantom used by Shepp and Logan (8). It is reproduced here as Fig. 1. Here we use 17 ellipsoids whose centers, axes, and incremental gray levels are given in Table 1. The parameters in Table 1 were chosen to be realistic and so that a particular section ($z = 0.381$) is consistent with the 11-ellipse phantom used by Shepp and Logan (8). Unfortunately, consistency required taking the NMR spin density of the skull as 2.0 whereas zero would probably be more realistic, since the skull has little water content. Front, side, and top views of the phantom are given in Figs. 2–4 and the $z = 0.381$ section is given in Fig. 1. Figure 5 shows the original phantom along one line $y = 0.23$, $z = 0.381$.

The area A of intersection of the plane $\xi \cdot u = t$ with the ellipsoid

$$\sum_{i=1}^{3}\left(\frac{(\xi-\xi_0)\cdot V_i}{a_i}\right)^2 \leq 1, \qquad \xi = (x,y,z) \quad (3.1)$$

centered at $\xi_0 = (x_0,y_0,z_0)$ with semiaxes a_1, a_2, a_3 along the orthonormal axes V_1, V_2, V_3 is given by

$$A = \pi a_1 a_2 a_3 (s^2 - \bar{t}^2)^+ S^{-3} \qquad (3.2)$$

where $\bar{t} = t - \xi_0 \cdot u$, $x^+ = \max(x,0)$, $u \cdot v = (u_x,u_y,u_z) \cdot (v_x,v_y,v_z) = u_x v_x + u_y v_y + u_z v_z$, and S is given by

$$S^2 = \alpha_1^2 a_1^2 + \alpha_2^2 a_2^2 + \alpha_3^2 a_3^2,$$

$$\alpha_i = u_i \cdot v_i, \ i = 1,2,3 \qquad (3.3)$$

We have used Eq. 3.2 in the FORTRAN program of Appendix A to calculate the planar projection data. Some of the experiments to be described also use slab projection data P_f. Here $\bar{P}_f(t,u;h)$ is the integral of f over the volume of the slab of thickness h centered at tu and normal to u, divided by h. This integral is the integral over $(t - (h/2), t + (h/2))$ of

A in Eq. 3.2. We show in Appendix B that the slab integral of f is the same as the plane integral of g, where g is the smoothed version of f obtained by integrating f over the surface of a sphere of radius $\frac{1}{2} h$, i.e., $P_g(t,u) = \bar{P}_f(t,u)$.

A typical projection of the head phantom (along the x-axis) is shown in Fig. 6, where $P(t,u)$ is plotted as a function of t and u is a unit vector along the positive x-axis. The second-difference filtered P, i.e., $Q(t,u)$ is shown in Fig. 7.

Figures 8–13 show reconstructions of f via Eq. 2.14 from plane data in the $z = 0.381$ plane for $m = n = 25$, 69, and 99, respectively. Figures 12 and 14–17 show reconstructions of f via Eq. 2.14 from slab data ($h = 3a$) for $m = n = 25$, 35, 49, 69. Each increment of $m = n$ roughly doubles the number of data points. These reconstructions may be compared with those of Shepp and Logan (8) and show that for $m = n = 49$ with (smooth) slab data or $m = n = 99$ with planar data, reconstructions comparable with the linear case are obtainable. This shows that the algorithmic aspects of NCT are achievable.

Figures 18 and 19 show a reconstruction in the same plane with planar integral projections, $m = n = 25$, but where the head phantom has been changed—namely, the high-contrast parts of the anatomy (ears, eyes, nose, mouth) which would cast tangents into the reconstruction plane have been "removed" (by having L in the program steps 360 and 460 skip over the values 3–8). The fact that a good reconstruction is now obtained with $m = n = 25$ shows that the optimal choice of the number of "views" m and n is phantom dependent, since excellent reconstructions can be obtained if there are no high-contrast objects in the phantom which cast tangents *into the region of interest* in the reconstruction. This problem has a familiar parallel in XCT (Appendix 1 in ref. 8) and is now well known. It is interesting that the human anatomy seems to be more friendly to XCT than to NCT in the above sense, but the experiments show that this unfriendliness can be overcome at the expense of obtaining more projection data. In this regard I have not put much effort into optimizing the choice of directions u_i along which data could be taken. I expect that significant improvements are possible here, although no set of directions gives a natural tesselation of the unit sphere, as is well known. It is likely that the sampling interval $a = 0.02$ in each of the experiments described in this section should be reduced for the case of plane data for better results. We have kept $a = 0.02$ for purposes of comparison with Shepp and Logan (8). For comparison with human dimensions, $a = 0.02$ corresponds to sampling roughly every 2 mm, or about 100 planes across the head in each direction. Increasing the resolution requires decreasing a, which in turn requires increasing m and n, however.

TABLE 1. *The center (x_0, y_0, z_0), the lengths (a_1, a_2, a_3) of the semiaxes, the incremental gray level (G) and the coordinates $(v_{11}, v_{12}, v_{13}, v_{21}, v_{22}, v_{23}, v_{31}, v_{32}, v_{33})$ of the three orthonormal axes of each of 17 ellipsoids corresponding to the head parts indicated.*

Head part[a]	x_0 / v_{12}	y_0 / v_{13}	z_0 / v_{21}	a_1 / v_{22}	a_2 / v_{23}	a_3 / v_{31}	G / v_{32}	v_{11} / v_{33}
1. Outer skull	0. 0.	0. 0.	0. 0.	0.7233 1.0000	0.9644 0.	1.27 0.	2.0000 0.	1.0000 1.0000
2. Inner skull	0. 0.	-0.0184 0.	-0.0185 0.	0.7008 1.0000	0.9246 0.	1.2241 0.	-0.9800 0.	1.0000 1.0000
3. Left eye	0.2583 0.	0.7534 0.	0. 0.	0.1270 1.0000	0.1270 0.	0.1270 0.	-1.0000 0.	1.0000 1.0000
4. Right eye	-0.2583 0.	0.7534 0.	0. 0.	0.1270 1.0000	0.1270 0.	0.1270 0.	-1.0000 0.	1.0000 1.0000
5. Nose	0. 0.	1.1398 0.	-0.1957 0.	0.1270 0.5446	0.3400 -0.8387	0.1700 0.	1.5000 0.8387	1.0000 0.5446
6. Mouth	0. 0.	0. 0.	-0.7620 0.	0.4575 1.0000	0.6099 0.	0.5080 0.	-1.0000 0.	1.0000 1.0000
7. Left ear	0.7076 -0.1085	-0.1378 -0.0865	-0.1905 0.1089	0.0635 0.9941	0.3175 0.	0.3175 0.0860	1.0000 -0.0094	0.9903 0.9963
8. Right ear	-0.7076 -0.1085	-0.1378 -0.0865	-0.1905 -0.1089	0.0635 0.9941	0.3175 0.	0.3175 -0.0860	1.0000 -0.0094	-0.9903 0.9963
9. Left small tumor	-0.0800 0.	-0.6050 0.	0.3810 0.	0.0460 1.0000	0.0230 0.	0.0230 0.	0.0100 0.	1.0000 1.0000
10. Center small tumor	0. 0.	-0.6050 0.	0.3810 0.	0.0230 1.0000	0.0230 0.	0.0460 0.	0.0100 0.	1.0000 1.0000
11. Right small tumor	0.0600 0.	-0.6050 0.	0.3810 0.	0.0230 1.0000	0.0460 0.	0.0230 0.	0.0100 0.	1.0000 1.0000
12. Old f	0. 0.	0.1000 0.	0.3810 0.	0.0460 1.0000	0.0460 0.	0.0460 0.	0.0100 0.	1.0000 1.0000
13. Old g	0. 0.	-0.1000 0.	0.1270 0.	0.2581 1.0000	0.2581 0.	0.2581 0.	0.0100 0.	1.0000 1.0000
14. Old e	0. 0.	0.3500 0.	0.3810 0.	0.2100 1.0000	0.2500 0.	0.2300 0.	0.0100 0.	1.0000 1.0000
15. Right ventricle	0.2200 -0.3090	0. 0.	0.3810 0.3090	0.1100 0.9511	0.3100 0.	0.2540 0.	-0.0200 0.	0.9511 1.0000
16. Left ventricle	-0.2200 -0.3090	0. 0.	0.3810 -0.3090	0.1600 0.9511	0.4100 0.	0.3810 0.	-0.0200 0.	-0.9511 1.0000
17. Blood clot	0.5600 -0.3381	-0.4000 0.2020	0.3810 0.3452	0.0300 0.9385	0.2000 0.	0.2000 0.1896	0.0300 -0.0697	0.9192 -0.9794

[a] Note that Nos. 12–14 refer to the tumors used in ref. 9 and indicated there by f, g, and e.

Figure 20 shows the reconstruction by the algorithm $\bar{f}$ of Eq. 2.18 from slab data $m = n = 69$ along the same line $y = 0.23$, $z = 0.381$ for purposes of comparison with Fig. 12 (algorithm f of Eq. 2.14). This is a less computionally convenient algorithm, so that we only computed the reconstruction along a line; but as can be seen from Fig. 20, the accuracy is poor compared to that of f in Fig. 12 where the same input data is used.

4. NOISE AND MEASUREMENT ERRORS

One noise source is Johnson noise in the coil which receives the NMR signal. This can be modeled in the same way as photon noise in XCT (7,8). Suppose each measured value of $P(t_i, \theta_j, \alpha_k)$ has an additive uncorrelated

random error η_{ijk} with mean zero and variance σ^2. Then the (biased) error in the reconstruction $\bar{f}(x,y,z)$ in Eq. 2.14 is

$$\frac{1}{4mn} \sum_{j=1}^{n} \sum_{k=0}^{m-1} \sin\theta_j \frac{1}{a^2} [2\eta_{ijk} - \eta_{l-1jk} - \eta_{l+1jk}] \quad (4.1)$$

approximately, where l depends on x,y,z and on j and k by Eqs. 2.14–2.15. The variance of the error in Eq. 4.1 at each point x,y,z is

$$\sigma_{\bar{f}}^2 = \frac{1}{16m^2n^2} \sum_{j=1}^{n} \sum_{k=0}^{m-1} \sin^2\theta_j \frac{1}{a^4} 6\sigma^2 = \frac{3\sigma^2}{16mna^4}. \quad (4.2)$$

To achieve the 0.5% density resolution claimed for XCT, i.e., $\sigma_{\bar{f}} < 0.005$, for the case where $m = n = 100$ and $a = 0.02$ (which corresponds to the experiments in Appendix
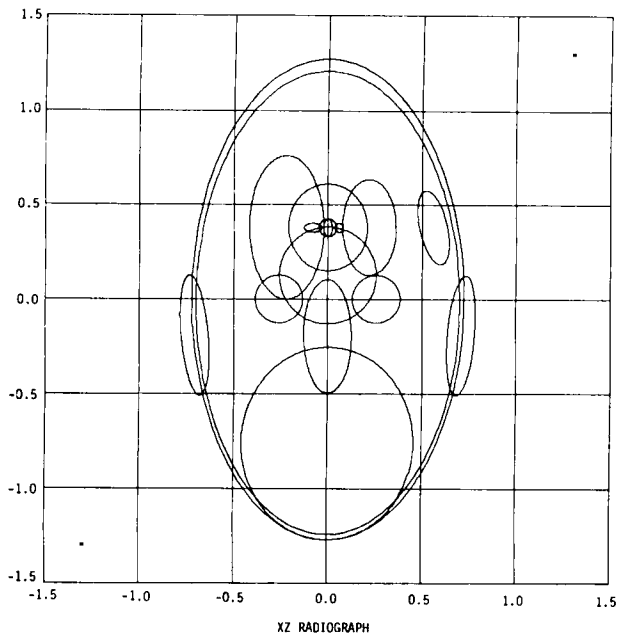
FIG. 2. Front view of phantom. The various body parts—nose, mouth, eyes, ears, ventricles, tumors, and skull—all have densities (not shown) given in Table 1.
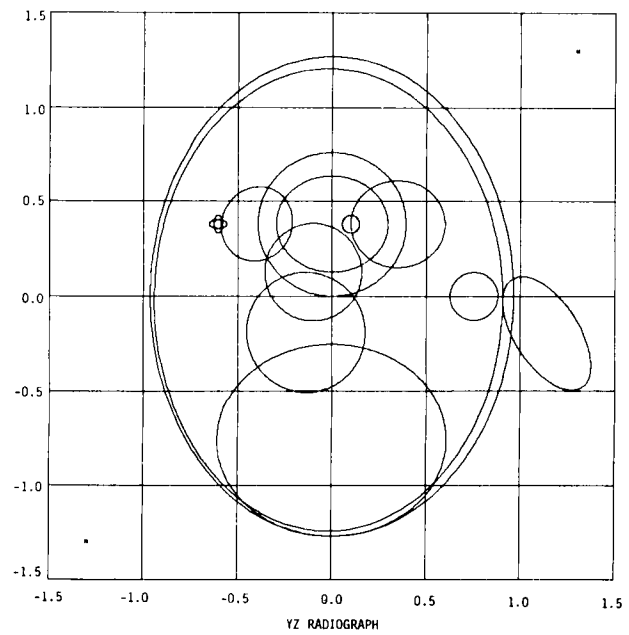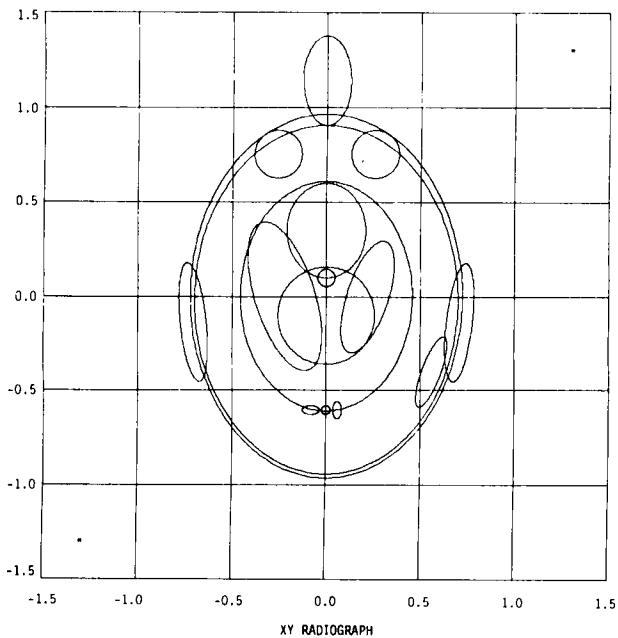

FIG. 3. Side view of phantom.
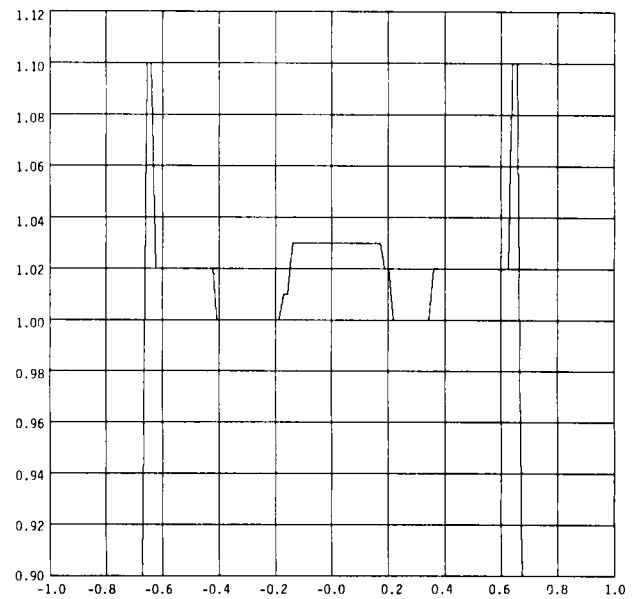

FIG. 4. Top view of phantom.

FIG. 5. Original phantom along the line $y = 0.23$, $z = 0.381$ truncated at 0.9 and 1.1. Note this line lies in the plane of the phantom used in ref. 8 and goes through the ventricles (density 1.0) and large tumor density (1.03) as well as the gray matter (1.02) (cf. Fig. 1).
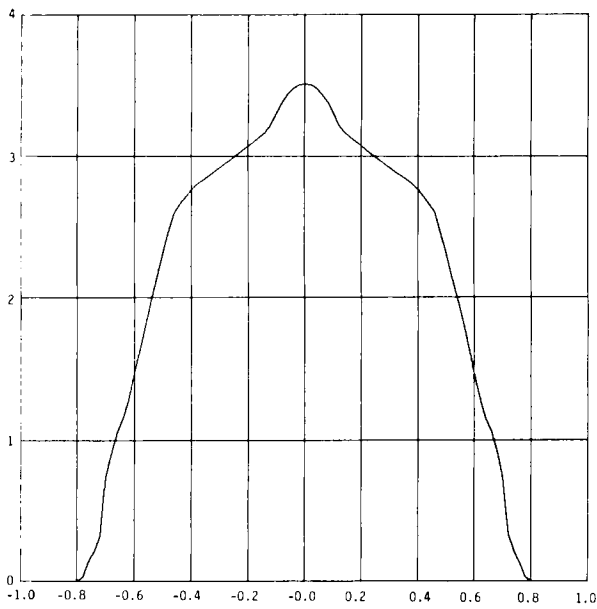
FIG. 6. Typical projection (onto the x-axis) of phantom.
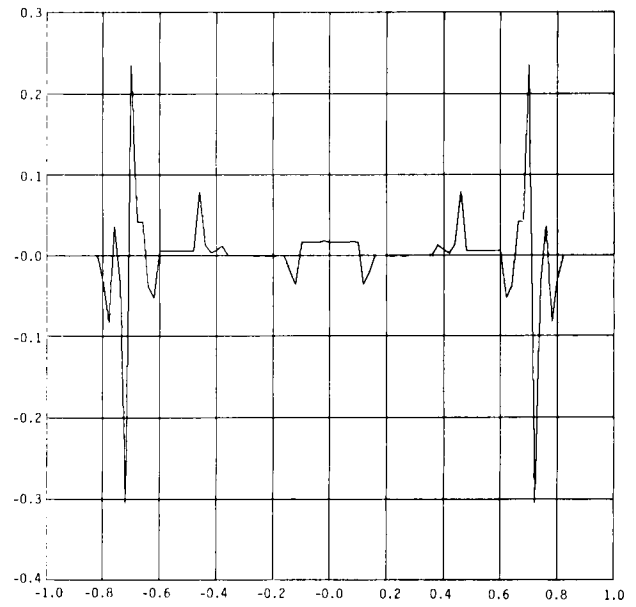
FIG. 7. Back-projected second differences of projections along x-axis.

FIG. 8. Reconstruction in same plane as Fig. 1 from planar data $m = n = 25$ with algorithm f of Eq. 2.14, truncated at 0.9 and 1.1. Very poor reconstruction.
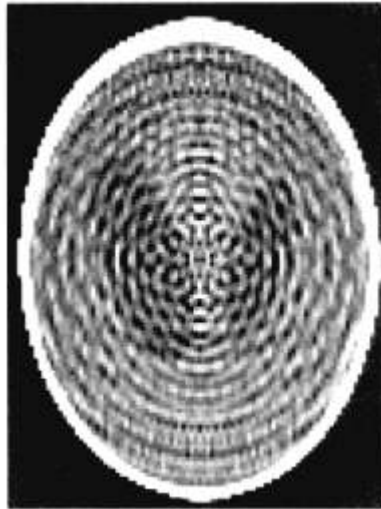
FIG. 9. Reconstruction under same conditions as Fig. 8 but plane data $m = n = 69$. Still a poor reconstruction.
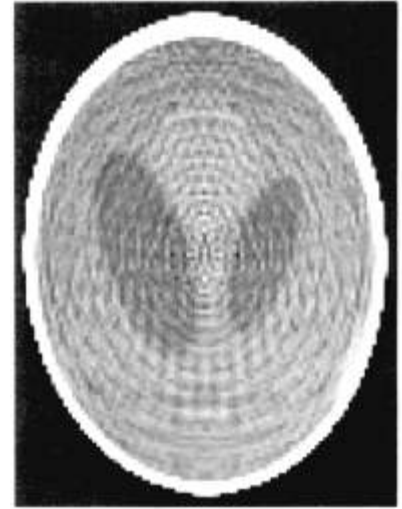
FIG. 10. Reconstruction under same conditions as Fig. 8 but plane data $m = n = 99$. Many artifacts, but note the three small tumors are visible.
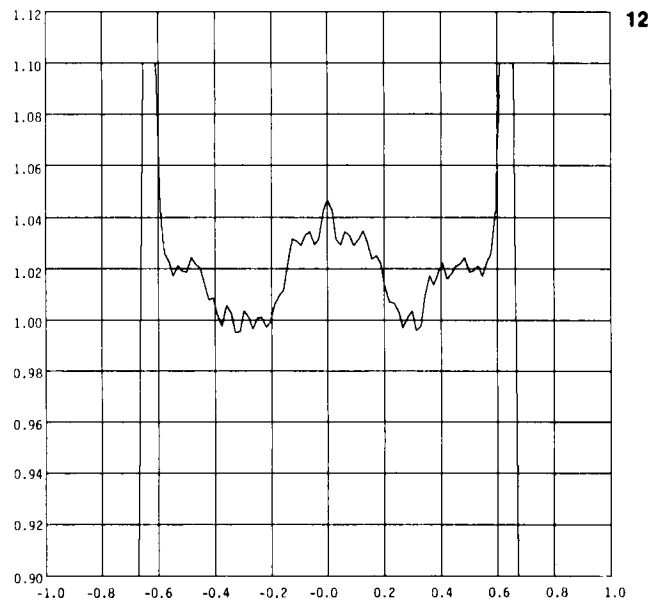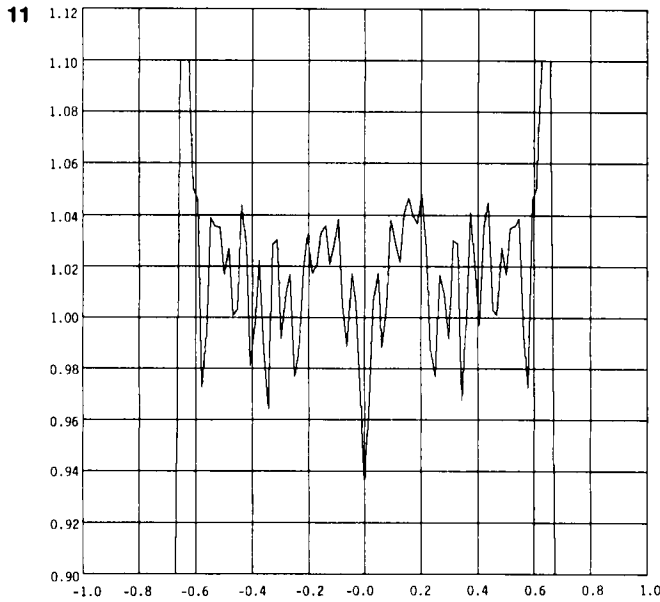
11

12

13
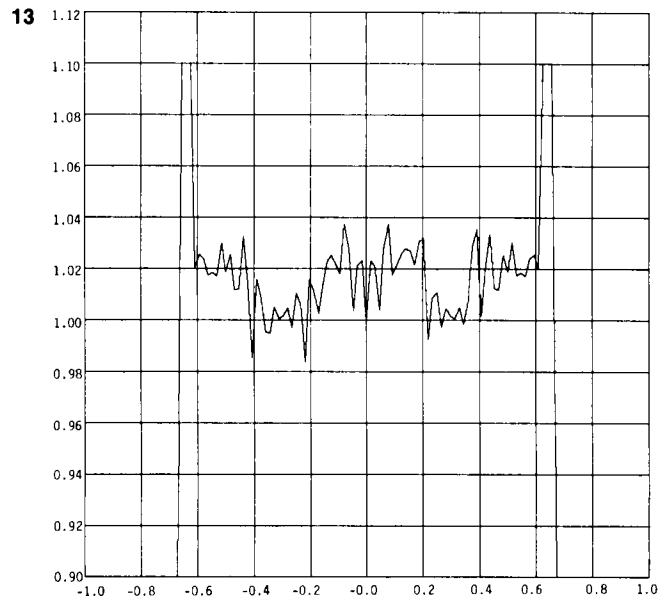
FIG. 11. Reconstruction along the same line as in Fig. 5 from planar data with $m = n = 69$ by algorithm f of Eq. 2.14 (cf. Fig. 5).

FIG. 12. Reconstruction along the same line as in Fig. 11 but with slab data $m = n = 69$ corresponding to a smoothed version of f (Appendix 2); (cf. Fig. 6).

FIG. 13. Same as Fig. 11 but with $m = n = 99$; plane data. Note that the three small tumors are visibly reconstructed (cf. Fig. 5).

A with 100 measurements across the unit sphere in each direction), we would require $\sigma < 4a^2(mn/3)^{1/2}\ 0.005 = 0.00046$. Since the central projections have values of roughly 2 in the experiment, this represents a relative error of 0.023%, a small tolerance on the Johnson noise. This severe tolerance, which may not be easily achievable, is a consequence of the second-order differentiation in the filter in the planar case. In the linear case, the filter requires only a first-order derivative (and Hilbert transform, which however does not amplify noise).

To reduce noise, filters may be used in the back-projection (at the expense of resolution), as was done by Shepp and Logan (8) in XCT. Indeed, if $Q(t,\theta,\alpha)$ in Eq. 2.16 is replaced by

$$Q_\phi(t,\theta,\alpha) = \sum_{l=-\infty}^{\infty} P(la,\theta,\alpha)\phi(t-la)a \qquad (4.3)$$

where ϕ is linear between $la < t < (l+1)a$ and

$$\dot{\phi}(\omega) = a \sum_{l=-\infty}^{\infty} \exp(-i\omega la)\phi(la) \doteq \omega^2, \qquad \text{small } |\omega| \qquad (4.4)$$

then we may form the approximation

$$f_\phi(x,y,z) = \frac{1}{4mn} \sum_{j=1}^{n} \sum_{k=0}^{m-1} \sin\theta_j Q_\phi(t,\theta_j,\alpha_k) . \qquad (4.5)$$

This should perform well, and the smaller $\int \dot{\phi}^2$, the better

FIG. 14. Reconstruction in same plane as Fig. 1 from slab data $m = n = 25$. Very poor reconstruction similar to Fig. 8, with which it should be compared.

FIG. 15. Reconstruction under same conditions as Fig. 14 but slab data $m = n = 35$.
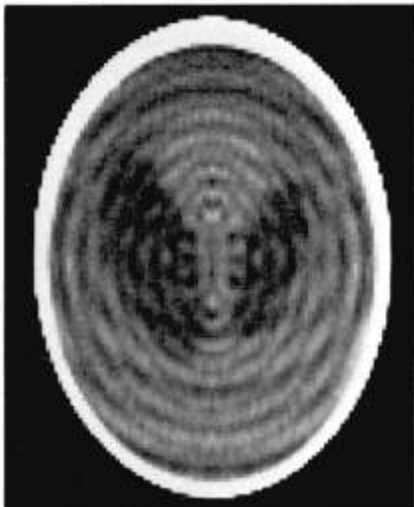

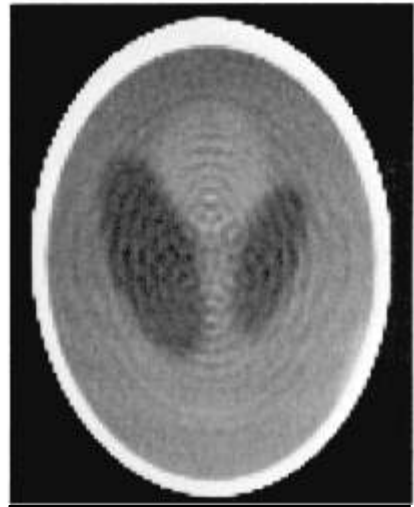**FIG. 16.** Reconstruction under same conditions as Fig. 14 but slab data $m = n = 49$.

FIG. 17. Reconstruction under same conditions as Fig. 14 but slab data $m = n = 69$. The three small tumors are not visible, probably because of the smoothing.

the noise reduction, since the argument in 4.1 gives in the same way

$$\sigma_\phi^2 = \frac{1}{16m^2n^2} \sum_{j=1}^{n} \sum_{k=0}^{m-1} \sin^2\theta_j \sigma^2 \sum_{l=-\infty}^{\infty} \phi^2(la)a^2$$

$$= \frac{\sigma^2}{32mn} a^2 \sum_{-\infty}^{\infty} \phi^2(la) \doteq \frac{\sigma^2 a}{32mn} \int \phi^2$$

$$= \frac{\sigma^2 a}{32mn} \frac{1}{2\pi} \int \dot\phi^2 . \tag{4.6}$$

The choice in Eq. 2.16 is $\phi = \phi_0(t)$, where

$$\phi_0(0) = \frac{2}{a^3}; \qquad \phi_0(\pm a) = -\frac{1}{a^3}$$

$$\phi_0(ka) = 0; \qquad k \geq 1. \tag{4.7}$$

On the other hand, the advantage of the latter choice is the ease of forming the convolution 2.16 involving only three terms.

A second measurement difficulty is due to the fact that the creation of a magnetic field gradient whose level surfaces are *exactly* planes has nonclosed flux lines and is thus impossible (because of the divergence theorem), although *in principle* it may be arbitrarily well approximated. How close tolerances are required on the curvature of the level surfaces? We consider in Appendix C replacing the integrals $P(t, u)$ over planes by integrals $P_R(t, u)$ over a sphere of (large) radius R which is perpendicular to u and passes through tu. For the function f_S, which is unity inside the unit sphere S and zero outside, we show that the reconstruction of f_S at the center of S from Eq. 2.13 using P_R instead of P has

FIG. 18. Reconstruction under same conditions as Fig. 8; plane data $m = n = 25$ but where the high-contrast out-of-plane objects (eyes, ears, nose, and mouth) have been removed and no longer cast tangents. Compare the quality of this reconstruction with that of Fig. 8. The three small tumors are clearly visible.

error $O(R^{-2})$. This gives at least qualitative reassurance that the level surfaces do not have to be exactly planar.

CONCLUSION

The experiment described in Section 3 and Fig. 18, where the nose, ears, eyes, and mouth are "temporarily removed," shows that from a mathematical viewpoint, reconstruction from plane integrals is as convenient and accurate as reconstructing from line integrals. However, from a medical point of view, the fact that the high-contrast body parts are not removable will cause some difficulties with any procedure which depends on algorithmic reconstruction from plane integrals, although with increased data the technique using the NMR gradient technique and the algorithm given here seems to hold much promise to compete with XCT.

APPENDIX A

The first program below generates NSAMP(= 101) planar integral projections P (statements 340–520), over each of NTH(=99) and NAL(=99) values of θ and α, from the 17 ellipsoids using (3.2) whose parameters are read in (160) from Table 1. The second difference $Q(530-550)$ of P is then back-projected (570–710) onto the plane $v_1 + r_1v_2 + r_2v_3 = (x,y,z)$ as r_1 and r_2 range in steps of size SF over ($-$SIZE,SIZE). To save execution time we only back-project onto points (x,y,z) inside the sphere of the projections $T(K)$, in this case this is the unit sphere. (This is the purpose of restricting IX in 670 and IY in 570.)

The second program below is identical to the first except for the choice of the number of angles (69 × 69) and the fact that each projection P is now the integral of f over a slab of thickness SLABWDTH (here taken to be three times the sampling distance in 110) computed in
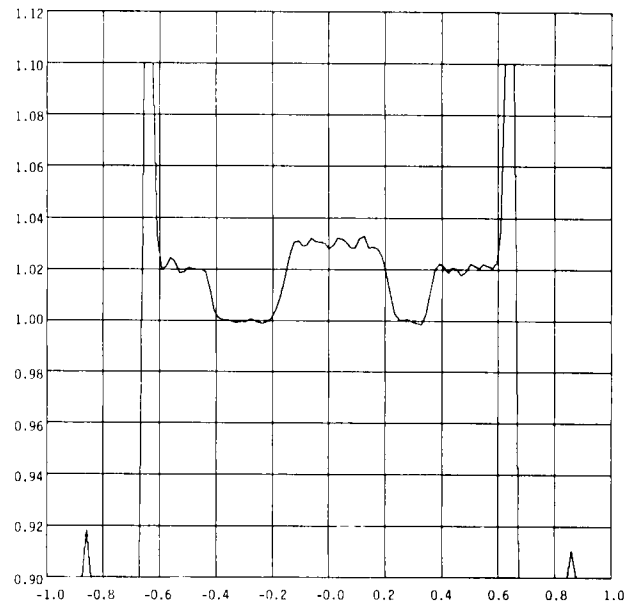

FIG. 19. Reconstruction along same line as in Fig. 5 from plane data with $m = n = 25$, but the high-contrast out-of-plane objects, which would otherwise cast tangents have been removed in calculating the projection data. Note the two blips in $|x| > 0.8$ indicating high oscillations (>0.9) outside the skull due to the casting of the tangents (cf. Fig. 5).
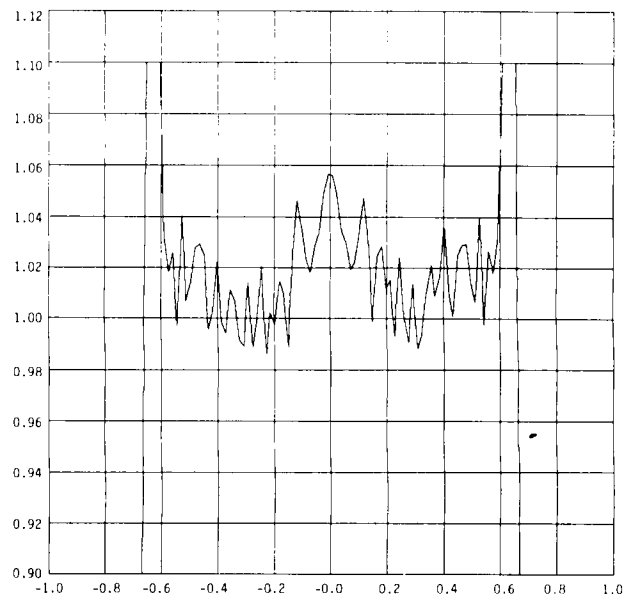

FIG. 20. Reconstruction along the same line as in Fig. 5 but using the algorithm $\tilde{f}$ in Eq. 2.18 instead of f in Eq. 2.14, $m = n = 69$ (cf. Figs. 5 and 12).

350–590, instead of a plane. As shown in Appendix B, this is equivalent to taking the planar integrals of a smoothed version of f.

APPENDIX B

As before we denote by $P_f(t,\theta,\alpha)$ the integral of $f =$

PROGRAM 1.

```
 40 >APAMETER  NSAMP=101,NTH=99,NAL=99,NREC=128
 50 DIMENSION  W(NREC,NREC),R(NREC)
 60 DIMENSION  X0(17),Y0(17),Z0(17),A(3,17),G(17),V(3,3,17)
 70 DIMENSION  AF(17),SUM(17),SQ(17),T0(17)
 80 DIMENSION  P(NSAMP),Q(NSAMP),T(NSAMP)
 90 DIMENSION  U(3),W1(3),V2(3),V3(3)
100 PI=3.14159265;PI2=2.*PI;CON=1./(4.*NTH*NAL)
110 ASA=2./(NSAMP-1.);ASA2=ASA*ASA;NSAMP1=NSAMP-1
120 V1(1)=0.;V1(2)=0.;V1(3)=.381
130 V2(1)=1.;V2(2)=0.;V2(3)=0.
140 V3(1)=0.;V3(2)=1.;V3(3)=0.
150 DO 2 L=1,17
160 READ(10,1000)  X0(L),Y0(L),Z0(L),A(1,L),A(2,L),A(3,L),
170| G(L),((V(I,J,L),J=1,3),I=1,3)
180 AF(L)=A(1,L)*A(2,L)*A(3,L)*PI*G(L)
190 2 CONTINUE
200 1000 FORMAT(8F8.4)
210 DO 5 K=1,NSAMP
220 5 T(K)=-1.+(K-1.)*2./(NSAMP-1.)
230 SIZE=1.;SF=2.*SIZE/NREC
240 DO 3 I=1,NREC
250 3 R(I)=SIZE*(-1.+(I-1.)*2./NREC)
260 SC=SQRT(1.-V1(1)**2-V1(2)**2-V1(3)**2)
270 IYMN=1.+.5*NREC*(1.-SO/SIZE);IYMN=MAX(IYMN,1)
280 IYMX=1.+.5*NREC*(1.+SO/SIZE);IYMX=MIN(IYMX,NREC)
290 DELX=V2(1)*SF;DELY=V2(2)*SF;DELZ=V2(3)*SF
300 DO 10 JTH=1,NTH
310 STH=SIN((JTH-.5)*PI/NTH);CTH=COS((JTH-.5)*PI/NTH)
320 DO 20 JAL=1,NAL
330 SAL=SIN((JAL-1.)*PI2/NAL);CAL=COS((JAL-1.)*PI2/NAL)
340CCCC   GET P
350 U(1)=STH*CAL;U(2)=STH*SAL;U(3)=CTH
360 DO 22 L=1,17
370 SUM(L)=0.
380 DO 23 M=1,3
390 23 SUM(L)=SUM(L)+((U(1)*V(M,1,L)+U(2)*V(M,2,L)+
400| U(3)*V(M,3,L))*A(M,L))**2
410 SQ(L)=SQRT(SUM(L))
420 T0(L)=U(1)*X0(L)+U(2)*Y0(L)+U(3)*Z0(L)
430 22 CONTINUE
440 DO 24 K=1,NSAMP
450 P(K)=0.
460 DO 25 L=1,17
470 TT=(T(K)-T0(L))**2
480 IF(SUM(L).LE.TT)GO TO 25
490 P(K)=P(K)+(SUM(L)-TT)*AF(L)/(SUM(L)*SQ(L))
500 25 CONTINUE;24 CONTINUE
510 IF(JTH.EQ.(NTH+1)/2.AND.JAL.EQ.1)PRINT,P
520CCCC   P GOT
```

generation of the projection data by planar integrals

```
530CC TAKE SECOND DIFFERENCES
540 DO 50 K=2,NSAMP-1
550 50 Q(K)=CON*(-P(K-1)-P(K+1)+2.*P(K))/ASA2
```

filtering

```
560 DEL=(DELX*STH*CAL+DELY*STH*SAL+DELZ*CTH)*(NSAMP-1.)/2.
570 DO 30 IY=IYMN,IYMX
580 SOO=SO-F(IY)*R(IY);IF(SOO.LE.0.)GO TO 30
590 SOO=SQRT(SOO)
600 IXMN=1.+.5*NREC*(1.-SOO/SIZE);IXMN=MAX(IXMN,1)
610 IXMX=1.+.5*NREC*(1.+SOO/SIZE);IXMX=MIN(IXMX,NREC)
620 X=V1(1)+R(IXMN)*V2(1)+R(IY)*V3(1)
630 Y=V1(2)+R(IXMN)*V2(2)+R(IY)*V3(2)
640 Z=V1(3)+R(IXMN)*V2(3)+R(IY)*V3(3)
650 TT=X*STH*CAL+Y*STH*SAL+Z*CTH
660 PP=1.+(TT+1.)*(NSAMP-1.)/2.-DEL
670 DO 40 IX=IXMN,IXMX
```

back-projection with linear interpolation

```
680 RF=R?+DEL
690 LL=RR;IF(LL.LE.1.OR.LL.GE.NSAMP1)GO TO 40
700 W(IX,IY)=W(IX,IY)+STH*(Q(LL)+(Q(LL+1)-Q(LL))*(RP-LL))
710 40 CONTINUE;30 CONTINUE
720 20 CONTINUE
730 10 CONTINUE
740 DO 60 IY=1,NREC
750 WRITE(12)  (W(IX,IY),IX=1,NREC)
760 IF(IY.EQ.65.OR.IY.EQ.80)PRINT,(W(IX,IY),IX=1,NREC),IY
770 60 CONTINUE
780 STOP;END
790$;EXECUTE
800$;PRMFL;10,R/W,,LAS/LMPDATA3
810$;PRMFL;12,R/W,,LAS/RPDP93
820$;LIMITS;160,50K,,2K
830$;ENDJOB
```

PROGRAM 2.

```
40  PARAMETER NSAMP=101,NTH=69,NAL=69,NREC=128
50  DIMENSION H(NREC,NREC),R(NREC)
60  DIMENSION X0(17),Y0(17),Z0(17),A(3,17),G(17),V(3,3,17)
70  DIMENSION AF(17),SUM(17),SQ(17),T0(17)
80  DIMENSION P(NSAMP),Q(NSAMP),T(NSAMP)
90  DIMENSION U(3),V1(3),V2(3),V3(3)
100 PI=3.14159265;PI2=2.*PI;CON=1./(4.*NTH*NAL)
110 SLABWDTH=3.*2./NSAMP;H=SLABWDTH;H2=H/2.
120 ASA=2./(NSAMP-1.);ASA2=ASA*ASA;NSAMP1=NSAMP-1
130 V1(1)=0.;V1(2)=0.;V1(3)=.381
140 V2(1)=1.;V2(2)=0.;V2(3)=0.
150 V3(1)=0.;V3(2)=1.;V3(3)=0.
160 DO 2 L=1,17
170 READ(10,1000) X0(L),Y0(L),Z0(L),A(1,L),A(2,L),A(3,L),
180L G(L),((V(I,J,L),J=1,3),I=1,3)
190 AF(L)=A(1,L)*A(2,L)*A(3,L)*PI*G(L)/H
200 2 CONTINUE
210 1000 FORMAT(8F8.4)
220 DO 5 K=1,NSAMP
230 5 T(K)=-1.+(K-1.)*2./(NSAMP-1.)
240 SIZE=1.;SF=2.*SIZE/NREC
250 DO 3 I=1,NREC
260 3 R(I)=SIZE*(-1.+(I-1.)*2./NREC)
270 S0=SQRT(1.-V1(1)**2-V1(2)**2-V1(3)**2)
280 IYMN=1.+.5*NREC*(1.-S0/SIZE);IYMN=MAX(IYMN,1)
290 IYMX=1.+.5*NREC*(1.+S0/SIZE);IYMX=MIN(IYMX,NREC)
300 DELX=V2(1)*SF;DELY=V2(2)*SF;DELZ=V2(3)*SF
310 DO 10 JTH=1,NTH
320 STH=SIN((JTH-.5)*PI/NTH);CTH=COS((JTH-.5)*PI/NTH)
330 DO 20 JAL=1,NAL
340 SAL=SIN((JAL-1.)*PI2/NAL);CAL=COS((JAL-1.)*PI2/NAL)
350CCCC   GET P
360 U(1)=STH*CAL;U(2)=STH*SAL;U(3)=CTH
370 DO 22 L=1,17
380 SUM(L)=0.
390 DO 23 M=1,3
400 23 SUM(L)=SUM(L)+((U(1)*V(M,1,L)+U(2)*V(M,2,L)+
410L U(3)*V(M,3,L))*A(M,L))**2
420 SQ(L)=SQRT(SUM(L))
430 T0(L)=U(1)*X0(L)+U(2)*Y0(L)+U(3)*Z0(L)
440 22 CONTINUE
450 DO 24 K=1,NSAMP
460 P(K)=0.
470 DO 25 L=1,17
480 TN=T(K)-T0(L)-H2
490 TP=TN+H
500 IF(TP.LT.-SQ(L))GO TO 25;IF(TN.GT.SQ(L))GO TO 25
510 QN=SUM(L)*TN-(TN*TN*TN)/3.;QP=SUM(L)*TP-(TP*TP*TP)/3.
520 IF(TP.GT.SQ(L))QP=2.*SUM(L)*SQ(L)/3.

530 IF(TP.LT.-SQ(L))QP=-2.*SUM(L)*SQ(L)/3.
540 IF(TN.GT.SQ(L))QN=2.*SUM(L)*SQ(L)/3.
550 IF(TN.LT.-SQ(L))QN=-2.*SUM(L)*SQ(L)/3.
560 P(K)=P(K)+AF(L)*(QP-QN)/(SUM(L)*SQ(L))
570 25 CONTINUE;24 CONTINUE
580 IF(JTH.EQ.(NTH+1)/2.AND.JAL.EQ.1)PRINT,P
590CCCC    P GOT
600CC TAKE SECOND DIFFERENCES
610 DO 50 K=2,NSAMP-1
620 50 Q(K)=CON*(-P(K-1)-P(K+1)+2.*P(K))/ASA2
630 DEL=(DELX*STH*CAL+DELY*STH*SAL+DELZ*CTH)*(NSAMP-1.)/2.
640 DO 30 IY=IYMN,IYMX
650 S00=S0*S0-R(IY)*R(IY);IF(S00.LE.0.)GO TO 30
660 S00=SQRT(S00)
670 IXMN=1.+.5*NREC*(1.-S00/SIZE);IXMN=MAX(IXMN,1)
680 IXMX=1.+.5*NREC*(1.+S00/SIZE);IXMX=MIN(IXMX,NREC)
690 X=V1(1)+R(IXMN)*V2(1)+R(IY)*V3(1)
700 Y=V1(2)+R(IXMN)*V2(2)+R(IY)*V3(2)
710 Z=V1(3)+R(IXMN)*V2(3)+R(IY)*V3(3)
720 TT=X*STH*CAL+Y*STH*SAL+Z*CTH
730 RP=1.+(TT+1.)*(NSAMP-1.)/2.-DEL
740 DO 40 IX=IXMN,IXMX
750 RR=RP+DEL
760 LL=RR;IF(LL.LE.1.OR.LL.GE.NSAMP1)GO TO 40
770 H(IX,IY)=H(IX,IY)+STH*(Q(LL)+(Q(LL+1)-Q(LL))*(RP-LL))
780 40 CONTINUE;30 CONTINUE
790 20 CONTINUE
800 10 CONTINUE
810 DO 60 IY=1,NREC
820 WRITE(12) (H(IX,IY),IX=1,NREC)
830 IF(IY.EQ.65.OR.IY.EQ.80)PRINT,(H(IX,IY),IX=1,NREC),IY
840 60 CONTINUE
850 STOP;END
860$:EXECUTE
870$:PRMFL:10,R/W,,LAS/LMPDATA3
880$:PRMFL:12,R/W,,LAS/RPDS69
890$:LIMITS:99,50K,,2K
900$:ENDJOB
```

generation
of the
projection
data by
slab
integrals

$f(x,y,z)$ over the plane $\mathcal{P}(t,\theta,\alpha)$ defined by $\sin\theta(x \cos\alpha + y \sin\alpha) + z \cos\theta = t$. Let $g = f * k$ be the three-dimensional convolution of f with a spherically symmetric kernel k,

$$g(x,y,z) = \iiint f(x - \bar{x}, y - \bar{y}, z - \bar{z})$$
$$k((\bar{x}^2 + \bar{y}^2 + \bar{z}^2)^{1/2}) \, d\bar{x} \, d\bar{y} \, d\bar{z}. \tag{B1}$$

We show that the plane projection of g, P_g satisfies

$$P_g(t,\theta,\alpha) = \int_{-\infty}^{\infty} P_f(t-s,\theta,\alpha)W(s) \, ds \tag{B2}$$

That is, P_g is a weighted, or filtered, version of P_f with filter weight $W(t)$, where

$$W(s) = 2\pi \int_s^\infty rk(r) \, dr . \tag{B3}$$

This may be inverted to give

$$k(s) = - \frac{1}{2\pi s} \frac{d}{ds} W(s) . \tag{B4}$$

If $\bar{P}_f(t,\mathbf{u};h)$ is the integral of f over the slab of thickness h centered at $t\mathbf{u}$ divided by h as defined in Section 3, then

$$\bar{P}_f(t,\mathbf{u};h) = \frac{1}{h} \int_{-h/2}^{h/2} P_f(t-s,\mathbf{u}) \, ds$$
$$= \int_{-\infty}^{\infty} P_f(t-s,\mathbf{u})W_h(s) \, ds \tag{B5}$$

where

$$W_h(s) = \begin{cases} 1/h, & -h/2 < s < h/2 \\ 0, & |s| > h/2 \end{cases} \tag{B6}$$

From Eq. B4 the corresponding smoothing kernel, k_h is

$$k_h(s) = \frac{1}{\pi h^2} \delta(s - h/2) \tag{B7}$$

where δ is unit point mass at zero. Thus $\bar{P}_f(t,\mathbf{u};h) = P_g(t,\mathbf{u})$, where $g = k_h * f$ is $(\pi h^2)^{-1}$ times the integral of f over the *surface* of a sphere of radius $h/2$ about any point. Thus the experiment in Section 3 involving slab-type projection data is the same as if one used plane projection data for a smoothed function $g = k_h * f$, which may be a more realistic model of a human head, i.e., the transitions between various head parts being perhaps not so sharp as the discontinuities of f.

Equation B2 is proved by several changes of variables as follows. Note first that

$$P_f(t,\theta,\alpha) = \iint_{-\infty}^{\infty} f(t\mathbf{u}+\xi\mathbf{v}_1+\eta\mathbf{v}_2) \, d\xi \, d\eta$$

$$= \iint_{-\infty}^{\infty} f(t \sin\theta \cos\alpha + \xi \cos\theta \cos\alpha$$
$$-\eta \sin\alpha, t \sin\theta \sin\alpha + \xi \cos\theta \sin\alpha$$
$$+\eta \cos\alpha, t \cos\theta - \xi \sin\theta) \, d\xi \, d\eta \tag{B8}$$

where $\mathbf{u} = (\sin\theta \cos\alpha, \sin\theta \sin\alpha, \cos\theta), \mathbf{v}_1 = (\cos\theta \cos\alpha, \cos\theta \sin\alpha, -\sin\theta)$, and $\mathbf{v}_2 = (-\sin\alpha, \cos\alpha, 0)$, since $\mathbf{v}_1, \mathbf{v}_2, \mathbf{u}$ are orthonormal.

Thus from Eq. B1,

$$P_g(t,\theta,\alpha) = \iiiint \int_{-\infty}^{\infty} f(t \sin\theta\cos\alpha + \xi \cos\theta \cos\alpha$$
$$- \eta \sin\alpha - \bar{x}, t \sin\theta \sin\alpha + \xi \cos\theta \sin \alpha$$
$$+ \eta \cos\alpha - \bar{y}, t \cos\theta - \xi \sin\theta - \bar{z})$$
$$k((\bar{x}^2+\bar{y}^2+\bar{z}^2)^{1/2}) \, d\bar{x} \, d\bar{y} \, d\bar{z} \, d\xi \, d\eta \tag{B9}$$

Introducing new variables ξ', η', s in place of $\xi, \eta, \bar{z}$ by

$$\xi = \xi'+c, \qquad \eta = \eta'+d, \qquad \bar{z} = s \cos\theta - c \sin\theta$$

where

$$c = (\bar{x} \cos\alpha + \bar{y} \sin\alpha - s \sin\theta)/\cos\theta$$
$$d = - \bar{x} \sin\alpha + \bar{y} \cos\alpha \tag{B10}$$

Eq. B9 becomes

$$P_g(t,\theta,\alpha) = \iiiint \int_{-\infty}^{\infty} f((t-s)\sin\theta \cos\alpha + \xi' \cos\theta \cos\alpha$$
$$-\eta' \sin\alpha, (t-s) \sin\theta \sin\alpha + \xi' \cos\theta \sin\alpha$$
$$+\eta' \cos\alpha, (t-s) \cos\theta - \xi' \sin\theta)$$
$$k((\bar{x}^2+\bar{y}^2+\bar{z}^2)^{1/2})J \, d\xi' \, d\eta' \, ds \, d\bar{x} \, d\bar{y} \tag{B11}$$

where the Jacobian $J = d\xi \, d\eta \, d\bar{z}/d\xi' \, d\eta' \, ds = 1/\cos\theta$.

Comparing the integral over ξ' and η' with Eq. B8, we have

$$P_g(t,\theta,\alpha) = \iiint_{-\infty}^{\infty} d\bar{x} \, d\bar{y} \, ds \, P_f(t-s,\theta,\alpha)$$

$$k((\bar{x}^2+\bar{y}^2+\bar{z}^2)^{1/2}) \frac{1}{\cos\theta}$$

$$= \int_{-\infty}^{\infty} P_f(t-s,\theta,\alpha)W(s) \, ds \tag{B12}$$

where

$$W(s) = \iint_{-\infty}^{\infty} d\bar{x} \, d\bar{y} \, k((\bar{x}^2+\bar{y}^2+\bar{z}^2)^{1/2} \frac{1}{\cos\theta} \tag{B13}$$

with $\bar{z}$ given by Eqs. B9 and B10. Finally, letting

$$\bar{x} \cos\alpha + \bar{y} \sin\alpha = u \cos\theta + s \sin\theta$$
$$- \bar{x} \sin\alpha + \bar{y} \cos\alpha = v \tag{B14}$$

and noting that $d\bar{x} \, d\bar{y}/du \, dv = \cos\theta$, we have

$$W(s) = \iint_{-\infty}^{\infty} du \, dv \, k((u^2+v^2+s^2)^{1/2}) \tag{B15}$$

which reduces to Eq. B3 on changing to polar coordinates $u = (r^2-s^2)^{1/2} \cos\phi, v = (r^2-s^2)^{1/2} \sin\phi$ since $du \, dv/dr \, d\phi = r$.

APPENDIX C

Here we suppose that instead of measuring $P_f(t,\mathbf{u})$, the integral of f over the plane $\mathcal{P}(t,\mathbf{u})$ whose normal from the origin is $t\mathbf{u}$, we suppose that the gradient field has curvature R at $t\mathbf{u}$. More precisely we suppose we measure $P_R(t,\mathbf{u})$ the integral of f over the spherical surface $S_R(t,\mathbf{u})$ which is centered at $(t+R)\mathbf{u}$ and has radius R, so that $S_R(t,\mathbf{u})$ passes through $t\mathbf{u}$ just as $\mathcal{P}(t,\mathbf{u})$ does.

Let us suppose that $f = 1$ inside a sphere S of radius ρ centered on the z-axis at $(0,0,z)$ and $f = 0$ outside the

sphere. Then the distance between the centers of the two spheres is, from the law of cosines,

$$\tau = (z^2+(t+R)^2 - 2z(t+R)\cos\theta)^{1/2} \qquad \text{(C1)}$$

where u makes an angle θ, $0 \le \theta \le \pi$, with the positive z axis. The projection $P_R(t,\theta,\alpha)$ along $S_R(t,u)$ is the area of that part of $S_R(t,u)$ inside S or

$$P_R(t,\theta,\alpha) = (\pi R/\tau)\,(a^2-(\tau-R)^2)^+ \qquad \text{(C2)}$$

for any α where $0 \le \alpha \le 2\pi$, as a simple calculation shows. Differentiating twice we get, for $|\tau-R| < a$,

$$P_R''(t,\theta,\alpha) = \pi R \left[2\,\frac{a^2-R^2}{\tau^3}\,(\tau')^2 + \left(\frac{R^2-a^2}{\tau^2} - 1\right)\tau'' \right]$$

$$\text{(C3)}$$

where $\tau'' = d^2\tau/dt^2 = -(\tau')^2/\tau + 1/\tau$ and $\tau' = d\tau/dt = (t+R-z\cos\theta)/\tau$. For the center of S, $t = z\cos\theta$ and $\tau^2 = R^2 + z^2\sin^2\theta$ and

$$\frac{\tau}{R} = 1 + O(R^{-2}), \qquad \tau' = 1 + 0(R^{-2}), \qquad \tau'' = O(R^{-2})$$

$$\text{(C4)}$$

so that

$$P_R''(z\cos\theta,\theta,\alpha) = -2\pi + O(1/R^2) \qquad \text{as } R \to \infty. \quad \text{(C5)}$$

From Eq. B13 we obtain that the approximate reconstruction of $f(0,0,z) = 1$ is $f_R(0,0,z) = 1 + O(1/R^2)$ as $R \to \infty$. Of course this argument is crude and hardly convincing that curved level surfaces in magnetic gradient fields do not cause serious problems, but there are many other methods that could be used to make corrections as long as the level surfaces are repeatable and known, i.e., remain constant each time the measurement $P(t,u)$ is taken.

ACKNOWLEDGMENT

REFERENCES

1. Radon J: Über die Bestimmung von Funktionen durch ihre Integralwerte längs gewisser Mannigfaltkeiten. *Ber Saech Akad Wiss* 69:262–277, 1917
2. Lauterbur PC: Magnetic resonance zeugmatography. *Pure Appl Chem* 40:149–157, 1974
3. Kumar A, Welti D, Ernst RR: NMR Fourier zeugmatography. *J Magn Reson* 18:69–83, 1975
4. Mansfield P, Maudsley AA: Planar spin imaging by NMR. *J Magn Reson* 27:101–119, 1977
5. Hinshaw WS, Andrew ER, Bottomley PA, Holland GN, Moore WS, Worthington BS: Display of cross sectional anatomy by nuclear magnetic resonance imaging. *Br J Radiol* 51:273–280, 1978
6. Budinger TF: Thresholds for physiological effects due to RF and magnetic fields used in NMR imaging. *IEEE Trans Nucl Sci* NS-26:2821–2825, 1979
7. Shepp LA, Stein JA: Simulated artifacts in computerized tomography. (In) Reconstructive Tomography in Diagnostic Radiology and Nuclear Medicine, ed. by M Ter-Pogossian, ME Phelps, GL Brownell, JR Cox Jr, DO Davis, RG Evens, Baltimore, University Park Press, 1974, pp 33–48
8. Shepp LA, Logan BF: The Fourier reconstruction of a head section. *IEEE Trans Nucl Sci* NS-21:21–43, 1974
9. Kellogg OD: Foundations of Potential Theory. New York, Fredrick Ungar, 1929 (reprinted by Dover, New York, 1953)
10. Shepp LA, Kruskal JB: Computerized tomography: The new medical x-ray technology. *Am Math Monthly* 85, 420–439